

Numerical analysis of propagation of macrocracks in 3D concrete structures affected by ASR

S. Moallemi^a and S. Pietruszczak*

Department of Civil Engineering, McMaster University, 1280, Main St W, Hamilton, Ontario, Canada

(Received June 12, 2017, Revised March 29, 2018, Accepted April 4, 2018)

Abstract. In this study an implicit algorithm for modeling of propagation of macrocracks in 3D concrete structures suffering from alkali-silica reaction has been developed and implemented. The formulation of the problem prior to the onset of localized deformation is based on a chemo-elasticity approach. The localized deformation mode, involving the formation of macrocracks, is described using a simplified form of the strong discontinuity approach (SDA) that employs a volume averaging technique enhanced by a numerical procedure for tracing the propagation path in 3D space. The latter incorporates a non-local smoothing algorithm. The formulation is illustrated by a number of numerical examples that examine the crack propagation pattern in both plain and reinforced concrete under different loading scenarios.

Keywords: 3D crack propagation; volume averaging; alkali-silica reaction; reinforced concrete

1. Introduction

One of the most important factors which can affect the durability of concrete structures is the alkali-silica-reaction (ASR). In recent decades several experimental and numerical studies have been conducted to understand this chemical process and to reduce the vulnerability of important structures such as dams and power plants. Although the chemistry behind the reaction is not completely understood, it has been generally accepted that in the presence of water the alkaline components of cement may react with silica present in the aggregate and produce a silica gel (Bazant and Meyer 2000). The experimental work has shown that the kinetics of this chemical process is a function of relative humidity, temperature, size and type of aggregates as well as the stress state (Pan *et al.* 2012, Berra *et al.* 2010, Diamond and Thaulow 1974, Multon *et al.* 2008). As the silica gel is formed and absorbs water, it can expand throughout the concrete mass and induce damage within its microstructure. First, the swelling gel fills the pores in the concrete skeleton and subsequently the pressure is exerted on constituents which leads to formation of microcracks and the reduction of concrete strength.

The research on development of continuum approaches describing the chemo-mechanical interaction started in the mid 1990's (Pietruszczak 1996, Capra and Bournazel 1998). Later, several derivative concepts were proposed that included both the continuum models (Ulm *et al.* 2000, Saouma and Perotti 2006) as well as micromechanical descriptions of ASR-induced deformation (Bazant and

Steffens 2000). It needs to be pointed out that there have only been a few attempts to perform large-scale simulations that involved the actual engineering structures. Most of these attempts (Saouma and Perotti 2006, Sellier *et al.* 2009, Pan *et al.* 2013, Winnicki *et al.* 2014) dealt mainly with the assessment of the influence of concrete expansion on the structural integrity, without accounting for the reaction-dependent degradation of material properties, and employed quite restrictive approaches for describing the onset and propagation of localized damage, particularly in compression regime.

Modeling of the progressive failure within the finite element framework has received a significant attention over the last few decades. A large number of studies have been conducted dealing with the onset and propagation of cracks in tensile regime (Hillerborg *et al.* 1976, Devloo 1991) as well as the formation of shear bands in compressive zones (Belytschko and Tabbara 1993, Zienkiewicz *et al.* 1995). The use of the standard finite element methodology has some limitations for modeling discontinuities. In order to overcome these limitations, the so-called strong discontinuity approach (SDA) was developed (Oliver 1996, Simo *et al.* 1993) in which the mesh sensitivity is reduced by embedding the displacement discontinues within the element. In this approach, a discontinuity function is added to the consistent part of the displacement field by employing new degrees of freedom in enhanced element (Sancho *et al.* 2007). Another scheme that incorporates the embedded discontinuity approach is known as eXtended Finite Element Method (XFEM). The latter involves the nodes enrichment within the enhanced element and employs the concept of partition of unity to update the related shape functions (Moës *et al.* 1999, Moës and Belytschko 2002, Sukumar *et al.* 2000). Several studies have been conducted to compare the accuracy different methodologies (cf. Oliver *et al.* 2006) and lately a significant amount of work was

*Corresponding author, Professor

E-mail: pietrusz@mcmaster.ca

^aPh.D.

E-mail: moallemi@mcmaster.ca

dedicated to the application of these methods to practical problems, e.g., the crack growth in concrete dams under gravitational and seismic loading (Pan *et al.* 2011, Pan *et al.* 2014).

In this study, an approach based on volume averaging within the region adjacent to the embedded discontinuity is examined. The procedure was developed in the early 1980's (Pietruszczak and Mroz 1981) and later modified by Pietruszczak (1999). Here, an enhanced methodology that stems from the recent work reported by Haghighat and Pietruszczak (2015, 2016) is employed that allows for a discrete representation of the crack propagation. The original approach outlined in Haghighat and Pietruszczak (2015) is extended here to 3D domain and the problem is reformulated to address the damage induced by continuing ASR. In the next section, an implicit formulation for chemo-mechanical interaction in concrete is outlined. Later on, in section 3, the constitutive relation in the presence of discontinuity is discussed. In section 4, the procedure for tracing the path of crack propagation in three-dimensional domain is explained and a smoothing algorithm is discussed. Finally, in the last section several numerical examples of damage propagation in plain and reinforced concrete structures subjected to various loading configurations, including chemical interaction and/or mechanical load, are presented.

2. Mathematical description of chemo-mechanical interaction in concrete

There are two main aspects involved in simulation of ASR in concrete, which are considered in a phenomenological framework: (i) the kinetics of the reaction and (ii) the degradation of mechanical properties of concrete. The former, i.e. the kinetics of the reaction, may be defined by introducing a scalar parameter ζ which is an explicit function of time and its evolution is affected by humidity, temperature and the confining pressure. In this study, humidity and temperature are considered constant, and an exponential relation (cf. Pietruszczak *et al.* 2013) is used to describe the kinetics of reaction, viz.

$$\zeta = 1 - \exp(-A_1 t) \quad (1)$$

where, A_1 is a material constant which controls the rate of the reaction. As it can be seen, ζ is defined within the interval $[0,1)$ whereas the reaction time varies within $[0, \infty)$. Degradation of concrete begins as soon as the macrocracks caused by the expansion of silica gels, start to appear. This affects both the deformation and strength properties. Restricting ourselves to the class of problems that involve failure in the *tensile* regime, the evolution laws for the modulus of elasticity, E , and tensile strength, f_t , may be expressed in the following form

$$E = E_0(1 - G_E \zeta) \quad f_t = f_{t0}(1 - G_f \zeta) \quad (2)$$

where, E_0 and f_{t0} are the initial values before the onset of the reaction and G_E and G_f are material constants that control the rate of degradation and can be identified from relevant experiments. Within the current framework, the chemical

strain $\boldsymbol{\varepsilon}_{\text{ASR}}$ is defined as a function of the kinetics of reaction and the confining pressure, i.e.

$$\boldsymbol{\varepsilon}_{\text{ASR}} = \frac{1}{3} [\mathbf{B}(\boldsymbol{\sigma}) \zeta \varepsilon_\infty] \mathbf{I}, \quad (3)$$

$$\mathbf{B}(\boldsymbol{\sigma}) = \begin{cases} \exp\left(-\frac{A_2 \text{tr}(\boldsymbol{\sigma})}{f_c}\right) & \text{tr}(\boldsymbol{\sigma}) < 0 \\ 1.0 & \text{tr}(\boldsymbol{\sigma}) > 0 \end{cases}$$

Here, ε_∞ is the maximum volumetric free expansion for a given alkali content, A_2 is a material constants, f_c denotes the compressive strength of concrete and \mathbf{I} is the identity tensor. Moreover, $\mathbf{B}(\boldsymbol{\sigma})$ describes the effect of confinement, which reduces the total ASR-related expansion, as reported in the literature (Larive 1998, Léger *et al.* 1996).

It is noted that the dependence of the kinetics of the reaction on the stress state may, in general, results in an anisotropic expansion. In this case, the problem may be reformulated by postulating that the strain tensor $\boldsymbol{\varepsilon}_{\text{ASR}}$ is co-linear with the stress tensor, i.e.

$$\boldsymbol{\varepsilon}_{\text{ASR}} = \varepsilon_\alpha \mathbf{e}^{(\alpha)} \otimes \mathbf{e}^{(\alpha)}; \quad \varepsilon_\alpha = \frac{1}{3} B_\alpha(\boldsymbol{\sigma}_\alpha) \varepsilon_\infty \zeta \quad (4)$$

where $\alpha=1,2,3$ and $\mathbf{e}^{(\alpha)}$ are the principal stress directions defined through an eigenvalue problem

$$(\boldsymbol{\sigma} - \lambda \mathbf{I}) : \mathbf{e}^{(\alpha)} = 0 \rightarrow \det(\boldsymbol{\sigma} - \lambda \mathbf{I}) = 0 \quad (5)$$

The constitutive relation may now be derived by invoking the framework of chemo-elasticity. In this case

$$\boldsymbol{\sigma} = \mathbb{D}^e : (\boldsymbol{\varepsilon} - \boldsymbol{\varepsilon}_{\text{ASR}}) \quad (6)$$

where \mathbb{D}^e is the elastic stiffness. By differentiating of Eq. (6) with respect to time and also taking into account the variation of material properties during the continuing reaction, one can write

$$\dot{\boldsymbol{\sigma}} = \mathbb{D}^e : (\dot{\boldsymbol{\varepsilon}} - \dot{\boldsymbol{\varepsilon}}_{\text{ASR}}) + \dot{\mathbb{D}}^e : [\mathbb{D}^e]^{-1} : \boldsymbol{\sigma} \quad (7)$$

where, the rate of change of elastic stiffness and the ASR-induced strain rate, Eq. (3), can be defined as

$$\dot{\mathbb{D}}^e = \frac{\partial \mathbb{D}^e}{\partial E} \frac{\partial E}{\partial \zeta} \frac{\partial \zeta}{\partial t}$$

$$\dot{\boldsymbol{\varepsilon}}_{\text{ASR}} = \frac{1}{3} \varepsilon_\infty \left[\zeta \frac{\partial \mathbf{B}(\boldsymbol{\sigma})}{\partial \boldsymbol{\sigma}} : \dot{\boldsymbol{\sigma}} + \mathbf{B}(\boldsymbol{\sigma}) \dot{\zeta} \right] \mathbf{I} \quad (8)$$

By substituting the above relation into Eq. (7), the stress rate can be expressed as

$$\dot{\boldsymbol{\sigma}} = [\mathbb{T}]^{-1} : \{ \mathbb{D}^e : (\dot{\boldsymbol{\varepsilon}} - \dot{\boldsymbol{\varepsilon}}_c) + \dot{\mathbb{D}}^e : [\mathbb{D}^e]^{-1} : \boldsymbol{\sigma} \} \quad (9)$$

$$\mathbb{T} = \left[\mathbb{I} + \frac{1}{3} \zeta \varepsilon_\infty \mathbb{D}^e : (\partial_\sigma \mathbf{B} \otimes \mathbf{I}) \right], \quad \dot{\boldsymbol{\varepsilon}}_c = \left(\frac{1}{3} \varepsilon_\infty \mathbf{B}(\boldsymbol{\sigma}) \dot{\zeta} \right) \mathbf{I}$$

In the numerical integration process, two different schemes can be employed, i.e., either explicit or implicit. In the explicit scheme, the stress state at time t_{n+1} can be determined directly by using the values of internal parameters at the previous time step t_n ; whereas in implicit scheme, the unknowns at time t_{n+1} can be found through an iterative process by satisfying constraints at the current time. Based on Eq. (9), the stress increment at each time step Δt can be approximated by the backward Euler scheme (Pietruszczak and Haghighat 2013). Thus

$$\begin{aligned} \boldsymbol{\sigma}_{t+\Delta t} &= \boldsymbol{\sigma}_t + \dot{\boldsymbol{\sigma}}_{t+\Delta t} \Delta t = \\ &= \boldsymbol{\sigma}_t + [\mathbb{T}]^{-1} : \{ \mathbb{D}^e : (\dot{\boldsymbol{\varepsilon}} - \dot{\boldsymbol{\varepsilon}}_c) \Delta t + \mathbb{D}^e : [\mathbb{D}^e]^{-1} : \boldsymbol{\sigma}_{t+\Delta t} \Delta t \} \end{aligned} \quad (10)$$

By solving for $\boldsymbol{\sigma}_{t+\Delta t}$ we have

$$\boldsymbol{\sigma}_{t+\Delta t} = \mathbb{Q}^{-1} : [\boldsymbol{\sigma}_t + \mathbb{D}^e : \mathbb{T}^{-1} : (\dot{\boldsymbol{\varepsilon}} - \dot{\boldsymbol{\varepsilon}}_c) \Delta t] \quad (11)$$

$$\mathbb{Q} = \mathbb{I} + \mathbb{T}^{-1} : \mathbb{D}^e : [\mathbb{D}^e]^{-1} \Delta t$$

where \mathbb{I} is the fourth order identity tensor and $\boldsymbol{\sigma}_t$ is the stress state at the beginning of increment.

In order to define the tangential stiffness operator, Eq. (9) may be written as

$$\begin{aligned} \Delta \boldsymbol{\sigma}_{t+\Delta t} &= \dot{\boldsymbol{\sigma}}_{t+\Delta t} \Delta t = \mathbb{T}^{-1} : \mathbb{D}^e : (\Delta \boldsymbol{\varepsilon} - \Delta \boldsymbol{\varepsilon}_c) + \\ &\mathbb{T}^{-1} : \mathbb{D}^e : [\mathbb{D}^e]^{-1} : (\boldsymbol{\sigma}_t + \Delta \boldsymbol{\sigma}_{t+\Delta t}) \end{aligned} \quad (12)$$

which, after some algebraic manipulations, leads to

$$\begin{aligned} \Delta \boldsymbol{\sigma}_{t+\Delta t} &= \mathbb{Q}^{-1} : \mathbb{T}^{-1} : \mathbb{D}^e : (\Delta \boldsymbol{\varepsilon} - \Delta \boldsymbol{\varepsilon}_c - \Delta t [\mathbb{D}^e]^{-1} : \boldsymbol{\sigma}_t) \\ &= \mathbb{D}_T : (\Delta \boldsymbol{\varepsilon} - \Delta \boldsymbol{\varepsilon}^*) \end{aligned} \quad (13)$$

where \mathbb{D}_T is the tangential operator and $\Delta \boldsymbol{\varepsilon}^*$ is the total strain generated by the chemical reaction.

3. Modelling of discontinuous deformation

In this section a mathematical description for a cracked domain subjected to chemical reaction is presented by incorporating a volume averaging scheme. The criterion for the crack initiation and the traction-separation law are discussed and an implicit formulation for updating the crack characteristics is developed.

3.1 Description of macrocrack propagation

Consider a domain contained within the volume Ω in which Γ_d denotes discontinuity surface that splits this domain into Ω^+ and Ω^- . The unit vector normal to crack is denoted by \mathbf{n} and points to Ω^+ .

Within this domain, the displacement field, $\mathbf{u}(\mathbf{x}, t)$ can be expressed as a combination of two continuous fields $\bar{\mathbf{u}}(\mathbf{x}, t)$ and $\tilde{\mathbf{u}}(\mathbf{x}, t)$ with the discontinuous jump function $H(\mathbf{x})$ (Oliver 1996)

$$\mathbf{u}(\mathbf{x}, t) = \bar{\mathbf{u}}(\mathbf{x}, t) + H(\mathbf{x}) \tilde{\mathbf{u}}(\mathbf{x}, t) \quad (14)$$

where, $H(\mathbf{x})$ is the Heaviside function which is equal to zero for all points in Ω^- and is equal to unity in the remaining part of the domain

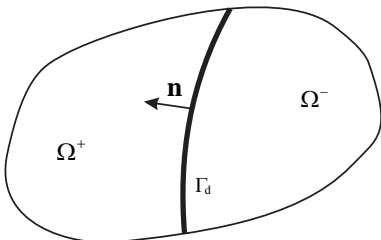


Fig. 1 Geometry of the problem

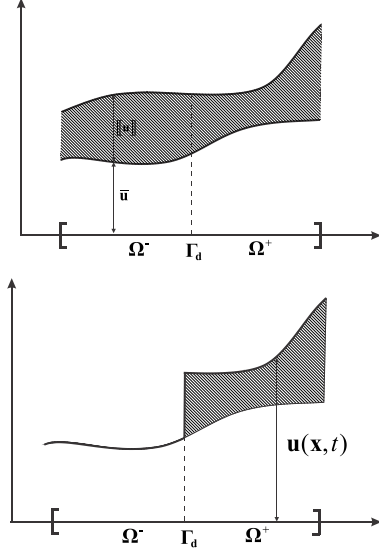


Fig. 2 Decomposition of displacement field for 1-D case

$$H(\mathbf{x}) = \begin{cases} 1 & \mathbf{x} \in \Omega^+ \\ 0 & \mathbf{x} \in \Omega^- \end{cases} \quad (15)$$

The terms defined in (14) are depicted in Fig. 2 to illustrate the displacement function in the context of a one-dimensional problem. Here, the dashed line indicates the position of discontinuity.

The strain tensor is calculated from the gradient of the displacement field (14)

$$\begin{aligned} \boldsymbol{\varepsilon} &= \nabla^s \mathbf{u}(\mathbf{x}, t) = \nabla^s \bar{\mathbf{u}}(\mathbf{x}, t) + \\ &\nabla^s \tilde{\mathbf{u}}(\mathbf{x}, t) H(\mathbf{x}) + \tilde{\mathbf{u}}(\mathbf{x}, t) \otimes \nabla^s H(\mathbf{x}) \end{aligned} \quad (16)$$

where the superscript s denotes the symmetric part of the gradient operator. Now, by averaging (16) over the considered volume yields (Haghighat and Pietruszczak 2015)

$$\begin{aligned} \frac{1}{\Delta \Omega} \int_{\Omega} \boldsymbol{\varepsilon} d\Omega &= \frac{1}{\Delta \Omega} \left\{ \int_{\Omega} \nabla^s \bar{\mathbf{u}}(\mathbf{x}, t) d\Omega \right. \\ &\left. + \int_{\Omega} \nabla^s \tilde{\mathbf{u}}(\mathbf{x}, t) H(\mathbf{x}) d\Omega + \int_{\Omega} \tilde{\mathbf{u}}(\mathbf{x}, t) \otimes \nabla^s H(\mathbf{x}) d\Omega \right\} \end{aligned} \quad (17)$$

The gradient of the Heaviside step function is defined by Dirac delta function as $\nabla H(x) = \delta_{\Gamma_d} \mathbf{n}$, so that Eq. (17) can be simplified to

$$\begin{aligned} \frac{1}{\Delta \Omega} \int_{\Omega} \boldsymbol{\varepsilon} d\Omega &= \frac{1}{\Delta \Omega} \left\{ \int_{\Omega} \nabla^s \bar{\mathbf{u}}(\mathbf{x}, t) d\Omega \right. \\ &\left. + \int_{\Omega} \nabla^s \tilde{\mathbf{u}}(\mathbf{x}, t) H(\mathbf{x}) d\Omega + \int_{\Omega} (\tilde{\mathbf{w}}(\mathbf{x}, t) \otimes \mathbf{n})^s d\Gamma_d \right\} \end{aligned} \quad (18)$$

where $\tilde{\mathbf{w}}(\mathbf{x}, t)$ indicates the displacement discontinuity. Thus, in terms of volume averages, the strain rate within the considered domain can be approximated by

$$\begin{aligned} \dot{\boldsymbol{\varepsilon}} &= \nabla^s \dot{\bar{\mathbf{u}}}(\mathbf{x}, t) + \left(\frac{\Delta \Omega^+}{\Delta \Omega} \right) \nabla^s \dot{\tilde{\mathbf{u}}}(\mathbf{x}, t) + \\ &\left(\frac{\Delta \Gamma_d}{\Delta \Omega} \right) (\dot{\tilde{\mathbf{w}}}(\mathbf{x}, t) \otimes \mathbf{n})^s \end{aligned} \quad (19)$$

Given the expression above, the total strain rate can be interpreted as a superposition of two parts, i.e., the strain rate in the intact material, $\dot{\hat{\boldsymbol{\varepsilon}}}$, and the strain rate in cracked zone, $\dot{\hat{\boldsymbol{\varepsilon}}}$, i.e.

$$\dot{\boldsymbol{\varepsilon}} = \dot{\hat{\boldsymbol{\varepsilon}}} + \dot{\hat{\boldsymbol{\varepsilon}}}; \text{ where } \dot{\hat{\boldsymbol{\varepsilon}}} = \nabla^s \left(\dot{\mathbf{u}}(\mathbf{x}, t) + \left(\frac{\Delta\Omega^+}{\Delta\Omega} \right) \tilde{\mathbf{u}}(\mathbf{x}, t) \right) \quad (20)$$

$$\dot{\hat{\boldsymbol{\varepsilon}}} = \chi(\dot{\mathbf{w}}(\mathbf{x}, t) \otimes \mathbf{n})^s$$

where χ denotes the ratio of the area of the crack to the referential volume. In order to satisfy the equilibrium condition, the traction along the crack surfaces should be continuous. Thus

$$\mathbf{n} \cdot \dot{\boldsymbol{\sigma}} = \dot{\mathbf{t}} = \mathbf{K} \dot{\mathbf{w}} \quad (21)$$

where, \mathbf{t} is the traction vector and \mathbf{K} is the stiffness of the fractured zone in the global coordinate system. Substituting Eq. (21) into the constitutive relation for intact material (13), we have

$$\mathbf{n} \cdot \mathbb{D}_T : (\dot{\hat{\boldsymbol{\varepsilon}}} - \dot{\boldsymbol{\varepsilon}}^*) = \mathbf{n} \cdot \mathbb{D}_T : (\dot{\boldsymbol{\varepsilon}} - \dot{\hat{\boldsymbol{\varepsilon}}} - \dot{\boldsymbol{\varepsilon}}^*) = \quad (22)$$

$$\mathbf{n} \cdot \mathbb{D}_T : (\dot{\boldsymbol{\varepsilon}} - \dot{\boldsymbol{\varepsilon}}^*) - \chi \mathbf{n} \cdot \mathbb{D}_T \cdot \mathbf{n} \dot{\mathbf{w}} = \mathbf{K} \dot{\mathbf{w}}$$

Consequently, by solving for $\dot{\mathbf{w}}$ in Eq. (22), the velocity discontinuity can be defined as

$$\dot{\mathbf{w}} = (\mathbf{S} \otimes \mathbf{n}) : [\mathbb{D}_T : (\dot{\boldsymbol{\varepsilon}} - \dot{\boldsymbol{\varepsilon}}^*)] \quad (23)$$

$$\text{where } \mathbf{S} = [\mathbf{K} + \chi \mathbf{n} \cdot \mathbb{D}_T \cdot \mathbf{n}]^{-1}$$

Finally, substituting Eq. (23) into the constitutive relation for intact material, the global relation between the total stress and strain rates can be obtained. The latter takes the form

$$\dot{\boldsymbol{\sigma}} = \mathbb{D}_T : (\dot{\boldsymbol{\varepsilon}} - \dot{\boldsymbol{\varepsilon}}^*) - \chi \mathbb{D}_T : (\mathbf{n} \otimes \dot{\mathbf{w}}) = \quad (24)$$

$$\mathbb{D}_T : [\mathbb{I} - \chi(\mathbf{n} \otimes \mathbf{S} \otimes \mathbf{n}) : \mathbb{D}_T] : (\dot{\boldsymbol{\varepsilon}} - \dot{\boldsymbol{\varepsilon}}^*) = \bar{\mathbb{D}}_T : (\dot{\boldsymbol{\varepsilon}} - \dot{\boldsymbol{\varepsilon}}^*)$$

3.2 Constitutive relation for macrocrack

In this section the constitutive law for the fractured zone is discussed which relates the traction rate to the velocity discontinuity. Over the last few decades, different types of relations have been proposed to define the characteristics of crack in different propagation modes. In order to obtain a symmetric stiffness operator for tensile cracks, the concepts of equivalent displacement, w_{eq} , and equivalent traction, t_{eq} , is used here as employed in the articles by Dumstorff and Meschke (2007), and/or Mariani and Perego (2003). The constitutive law is taken in the form

$$t_{eq} = \hat{K} w_{eq}, \quad w_{eq} = \sqrt{w_n^2 + \beta^2 (w_{s1}^2 + w_{s2}^2)} \quad (25)$$

where \hat{K} is defined as

$$\hat{K} = K_0 \frac{d_0}{d} \exp\left(-\frac{f_t}{G_f} (d - d_0)\right) \quad (26)$$

In the equations above, the scalar parameter β controls the effect of shear sliding on the equivalent traction, while

w_n and w_s denote displacement jumps in the normal and tangential direction, respectively, in the local coordinate system attached to the crack. Furthermore, K_0 is the initial stiffness, d_0 denotes the equivalent displacement at which the attenuation of stiffness starts, d is the maximum equivalent displacement during the loading history, f_t represents the tensile strength and G_f is the fracture energy. It is noted that for $\beta=0$ the stiffness operator \hat{K} has the same form as that suggested by Wells and Sluys (2001).

In order to obtain an explicit form of the constitutive relation in terms of normal and tangential tractions, the concept of total equivalent work is implemented, viz.

$$t_{eq} \dot{w}_{eq} = t_n \dot{w}_n + t_{s1} \dot{w}_{s1} + t_{s2} \dot{w}_{s2} \quad (27)$$

By evaluating the rate of w_{eq} in Eq. (25) and using relation (27), we have

$$t_{eq} \left(\frac{w_n}{w_{eq}} \dot{w}_n + \beta^2 \frac{w_{s1}}{w_{eq}} \dot{w}_{s1} + \beta^2 \frac{w_{s2}}{w_{eq}} \dot{w}_{s2} \right) = t_n \dot{w}_n + t_{s1} \dot{w}_{s1} + t_{s2} \dot{w}_{s2} \quad (28)$$

By comparing the two sides of Eq. (28) and using (25) one can write

$$t_n = \hat{K} w_n, \quad t_{s1} = \beta^2 \hat{K} w_{s1}, \quad t_{s2} = \beta^2 \hat{K} w_{s2} \quad (29)$$

In order to define now the second order tensor \mathbf{K} , viz. Eq. (21), the rate form of Eq. (29) should be employed, i.e.

$$\dot{t}_n = \dot{\hat{K}} w_n + \hat{K} \dot{w}_n; \quad \dot{t}_{s1} = \beta^2 (\dot{\hat{K}} w_{s1} + \hat{K} \dot{w}_{s1});$$

$$\dot{t}_{s2} = \beta^2 (\dot{\hat{K}} w_{s2} + \hat{K} \dot{w}_{s2}) \quad (30)$$

For an active loading process $\dot{d} > 0$, using relations (26) and (30) and noting that $d = w_{eq}$, leads to a following expression for the stiffness tensor \mathbf{K}

$$\mathbf{K} = \hat{K} \left(\frac{G_f + w_{eq} f_t}{w_{eq}^2 G_f} \right) \times \begin{bmatrix} \frac{w_{eq}^2 G_f}{G_f + w_{eq} f_t} - w_n^2 & -\beta^2 w_n w_{s1} & -\beta^2 w_n w_{s2} \\ -\beta^2 w_n w_{s1} & \frac{\beta^2 w_{eq}^2 G_f}{G_f + w_{eq} f_t} - \beta^4 w_{s1}^2 & -\beta^4 w_{s1} w_{s2} \\ -\beta^2 w_n w_{s2} & -\beta^4 w_{s1} w_{s2} & \frac{\beta^2 w_{eq}^2 G_f}{G_f + w_{eq} f_t} - \beta^4 w_{s2}^2 \end{bmatrix} \quad (31)$$

Following the same procedure for the case of unloading ($\dot{d} < 0$), one obtains

$$\mathbf{K} = \hat{K} \begin{bmatrix} 1 & 0 & 0 \\ 0 & \beta^2 & 0 \\ 0 & 0 & \beta^2 \end{bmatrix} \quad (32)$$

3.3 Implicit integration for updating the crack characteristics

During an active loading process, the mechanical

response of the macrocrack can be traced using an implicit integration scheme, similar to that outlined by Haghghat and Pietruszczak (2015). In this case, the following residuals at increment n and iteration k are defined

$$\mathbf{R}_1^k = \mathbf{n} \cdot \dot{\boldsymbol{\sigma}}_n^k - \mathbf{K}\dot{\mathbf{w}}_n^k = \mathbf{0} \quad (33)$$

$$\mathbf{R}_2^k = \dot{\boldsymbol{\sigma}}_n^k - \mathbb{D}_T : (\dot{\boldsymbol{\epsilon}} - \dot{\boldsymbol{\epsilon}}^*) + \chi \mathbb{D}_T : (\mathbf{n} \otimes \dot{\mathbf{w}}_n^k) = \mathbf{0}$$

Employing Newton-Raphson algorithm, these can be approximated as

$$\mathbf{R}_1^{k+1} \approx \mathbf{R}_1^k + \frac{\partial \mathbf{R}_1^k}{\partial \boldsymbol{\sigma}} : \delta \boldsymbol{\sigma}^k + \frac{\partial \mathbf{R}_1^k}{\partial \mathbf{w}} \delta \mathbf{w}^k = \mathbf{0} \quad (34)$$

$$\mathbf{R}_2^{k+1} \approx \mathbf{R}_2^k + \frac{\partial \mathbf{R}_2^k}{\partial \boldsymbol{\sigma}} : \delta \boldsymbol{\sigma}^k + \frac{\partial \mathbf{R}_2^k}{\partial \mathbf{w}} \delta \mathbf{w}^k = \mathbf{0}$$

Substituting Eqs. (33) into (34) yields

$$\begin{aligned} \delta \mathbf{w}^k &= [\mathbf{K} + \chi \mathbf{n} \cdot \mathbb{D}_T \cdot \mathbf{n}]^{-1} (\mathbf{R}_1^k - \mathbf{n} \cdot \mathbf{R}_2^k) \\ \delta \boldsymbol{\sigma}^k &= -\chi \mathbb{D}_T : (\mathbf{n} \otimes \delta \mathbf{w}^k) - \mathbf{R}_2^k \end{aligned} \quad (35)$$

This procedure is continued until the residuals given in Eq. (33) vanish. Note that at the end of each iteration the updated values of stress and crack opening are given by

$$\begin{aligned} \boldsymbol{\sigma}_n^k &= \boldsymbol{\sigma}_n + \Delta \boldsymbol{\sigma}_n^k; & \Delta \boldsymbol{\sigma}_n^k &= \Delta \boldsymbol{\sigma}_n^{k-1} + \delta \boldsymbol{\sigma}_n^k \\ \mathbf{w}_n^k &= \mathbf{w}_n + \Delta \mathbf{w}_n^k; & \Delta \mathbf{w}_n^k &= \Delta \mathbf{w}_n^{k-1} + \delta \mathbf{w}_n^k \end{aligned} \quad (36)$$

4. Three-dimensional crack propagation strategy

Referring to Jäger *et al.* (2008), there are three different approaches for tracing the crack path in 3D problems, i.e., level set, global tracking and local tracking. Owing to high computational cost of the first two schemes, the local tracking approach is employed in this study. In what follows, the main strategy is presented first for 2D case and then extended to 3D applications. Referring to Gasser and Holzapfel (2006), each crack is composed of a number of line segments which pass through elements and cut the sides at two points. The location of these points is stored in order to trace the crack and also to define the characteristic length parameter, χ , Eq. (20). At the end of each load increment, two steps are required to update the crack configuration; the first one involves checking the failure criterion for the elements next to the crack tip, and the second deals with identifying elements which satisfy failure condition to establish a new crack within the domain. In the former case, the cut side of the crack tip element is searched to find the new candidate crack element with the joint side (Fig. 3). If the failure condition is satisfied, the crack will propagate from the cut point (former crack tip) in the direction perpendicular to maximum tensile stress (for tensile fracture) to form a new crack tip.

This methodology has been extensively used, as evidenced in the existing literature (Manzoli and Shing 2006, Linder and Armero 2007). In analogy to 2D case, a similar procedure can be implemented for three dimensional problems, whereby the triangular elements are replaced by a tetrahedral mesh and the crack segment is replaced by the crack surface. Fig.4 depicts the cracked elements containing

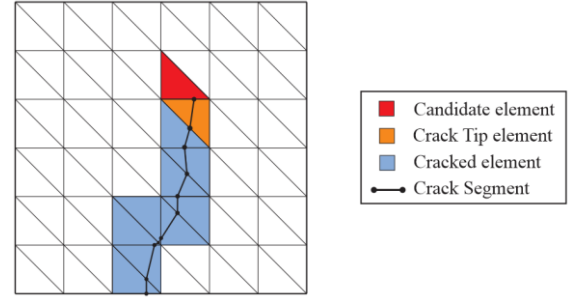


Fig. 3 Crack propagation algorithm in 2D problems

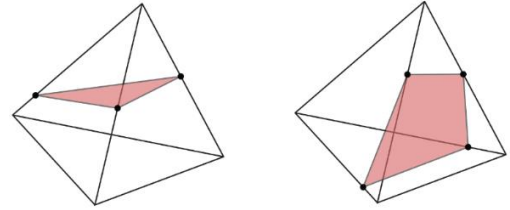


Fig. 4 Crack surface in tetrahedral elements

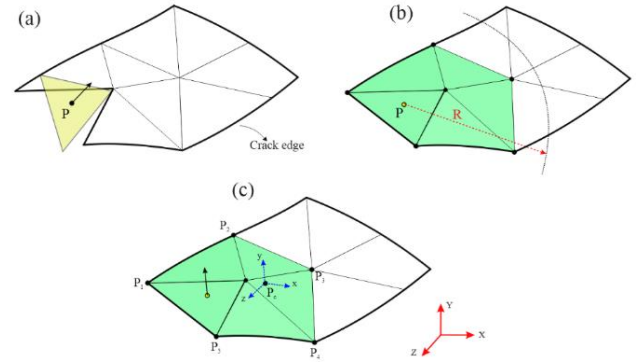


Fig. 5 (a) Predicted direction for new crack surface (b) detecting elements in the vicinity of point P (c) modified normal direction to update crack surface

a failure plane. As the crack propagates, new tip-facets are identified and the neighbor elements become candidate elements for the next crack tip. As pointed out by Gasser and Holzapfel (2006), using local tracking algorithm without modification cannot give reliable results, thereby a smoothing algorithm is employed here to overcome the difficulties related to 3D crack propagation. A brief review of this procedure is given below.

The geometric scheme is shown in Fig. 5, where the bold lines define the crack edge and the thin lines are associated with cut surface in cracked elements. As the failure criterion is met in the front element, the direction of propagation is calculated and compared with that in the adjacent element. In some cases, the obtained crack segment may not be consistent with the crack surface, hence the smoothing is imposed to modify the crack propagation direction. It is noted that crack surface embedded in the new crack tip elements initiates from the point obtained as an average of cut facets in neighbor elements (point P). To adjust the normal direction, all points within the radius R of the current crack tip, which formed other crack surfaces, are picked to define a new surface to

approximate normal vector at any point of interest.

In the first step, the centroid of the new surface, referred to as P_c , is obtained. To define the equation of the crack surface, the local coordinate system is introduced and placed at the centroid point. As discussed by Gasser and Holzapfel (2006), to obtain the local axis, the following covariance tensor is defined

$$\mathbf{T} = \sum_{i=1:n_p} (P_i - P_c) \otimes (P_i - P_c) \quad (37)$$

where P_i is the location of cut points in the crack surface and n_p defines number of these points. The eigenvectors of this tensor define the local coordinate system at P_c . To achieve more accuracy, the second order approximation is considered for the surface, i.e.

$$z = a_0 + a_1x + a_2y + a_3x^2 + a_4y^2 + a_5xy \quad (38)$$

and the coefficients of approximation a_i , are determined by minimizing the difference between z and z_i , where the latter is the value of the function in Eq. (38) at point P_i . Therefore, the problem can be formulated as a least square problem

$$\text{minimize } \Psi = \sum_{i=1:n_r} (z - z_i)^2 \quad \text{solve for } a_i \quad (39)$$

Once the solution is obtained, the direction of the normal at point P can be determined by calculating the gradient of (38). Note that this direction is defined in the local coordinate system and it should be transformed to the global frame of reference.

5. Numerical examples

In this section several numerical examples are provided to demonstrate the robustness of the approach described in Sections 2-3. The governing constitutive relations, together with the proposed scheme for tracing the crack propagation, have been implemented into Abaqus FEA software. It should be pointed out that although the numerical analysis presented here has been conducted in 3D, all examples can be treated as 2D problems. In fact, the cracks propagate in quasi-3D mode, i.e., crack surfaces remain plane and undistorted along the thickness. The verification of the procedure for tracing the crack path in the context of real 3D geometry is provided in the recent paper by Moallemi and Pietruszczak (2017). In that article, a three-point bending test is simulated in which the fracture pattern involves a progressive twisting of the crack surface and its propagation in the direction aligned with that of the prescribed displacements.

5.1 L-Shape concrete panel

In the first example the crack trajectory is investigated in an L-shaped pure concrete panel. The geometry and the FE discretization are shown in Fig. 6. The bottom of the L-shaped specimen is fixed and the vertical displacement is applied incrementally to the left edge of the panel. This example simulates an experimental set up of Winkler *et al.*

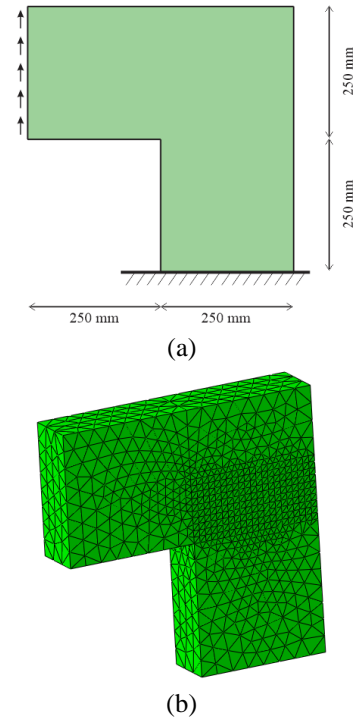


Fig. 6 (a) Geometry and boundary condition of problem; (b) Finite element discretization

(2001) and was previously employed as a benchmark for examining the accuracy of different numerical approaches for modeling of the crack propagation (Dumstorff and Meschke 2007, Jäger *et al.* 2008). The material is considered here as elastic-brittle and the assumed properties are

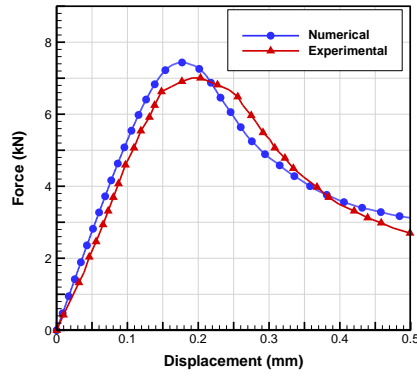
$$E=25.85 \text{ (GPa); } \nu=0.18; f_t=2.7 \text{ (MPa); } G_f=0.1 \text{ (N/nm)}$$

The thickness of the panel is 100 mm and the value of β given in Eq. (25) is set to 1.5 in order to consider the effects of tangential displacement in cohesive law. Three dimensional linear tetrahedral elements are used to discretize the structure, as depicted in Fig. 6. The loading is imposed incrementally and as the principal stress reaches f_t , the crack initiates and progressively grows as the load increases. By applying the strategy described in the previous section, a smooth crack path is obtained, as shown in Fig. 7 which is similar to the results presented by Dumstorff and Meschke (2007). In addition, the load displacement curve for the panel is compared here with the experimental data given in the article by Winkler *et al.* (2001); clearly the results of simulations incorporating the proposed methodology are quite accurate.

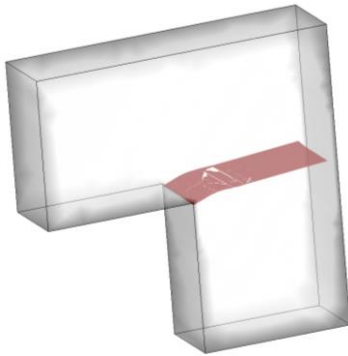
5.2 Crack propagation in reinforced concrete beam

The next example studied here is involves a reinforced concrete beam subjected to a three-point bending. This problem was studied experimentally by Bresler and Scordelis (1963) using different ratios of reinforcements. The reinforcement is considered here in a discrete way using the standard Abaqus library.

Fig. 8 shows the geometry of the problem. Four



(a)



(b)

Fig. 7 (a) load-displacement curve; (b) crack path

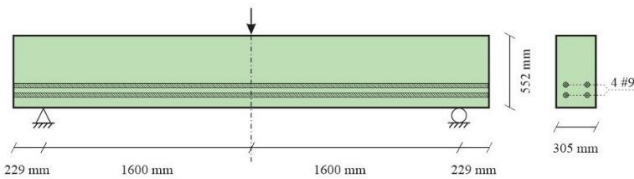


Fig. 8 Geometry of simply supported reinforced concrete beam

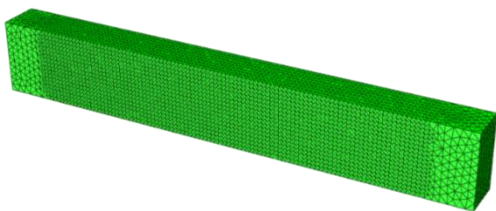


Fig. 9 FE discretization by tetrahedral elements

longitudinal high strength steel bars #9 (#29 in metric unit) are placed within the concrete in two layers and the vertical load is applied incrementally to the top surface of the beam. The finite element discretization is provided in Fig. 9 and the material properties of steel and concrete are given below Steel:

$$E_s = 200 \text{ GPa}, \quad \nu = 0.2, \quad f_y = 555 \text{ MPa}$$

Concrete:

$$E_c = 23.8 \text{ GPa}, \quad \nu = 0.18, \quad f_t = 1.82 \text{ MPa}, \\ G_f = 0.1 \text{ N/mm}, \quad \beta = 0.1$$

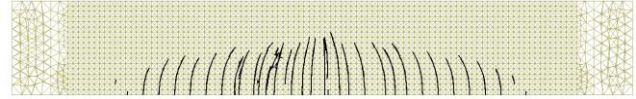


Fig. 10 Crack path in beam after 2 mm deflection

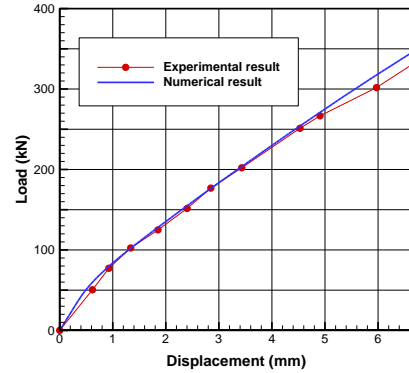


Fig. 11 Load displacement curve for reinforced concrete beam

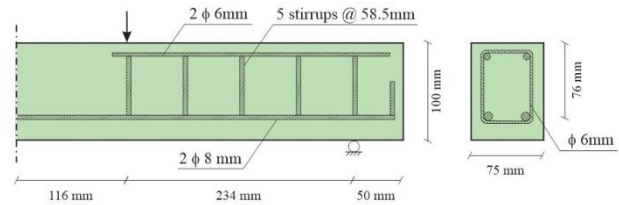


Fig. 12 Geometry of the right half of concrete beam

As the load increases, the cracks initiate first at the mid-span of the beam as soon as the maximum principal stress reaches the strength of concrete. Due to the presence of reinforcement in the tensile region of the beam, the cracks cannot propagate further since the steel bars resist the crack opening. Consequently, other flexural cracks form at the bottom and propagate upwards as shown in Fig. 10.

In Fig. 11, the load-displacement response for the beam is compared with the experimental data reported by Bresler and Scordelis (1963). It is clear that the numerical results are fairly consistent here with the experimental evidence. Note that within the considered range of external load, the steel bars didn't reach the yield point, so that the mechanical characteristic remains stable.

5.3 ASR in reinforced concrete beam

In the last example dealing with the tensile fracture, the response of reinforced concrete beam subjected to ASR is examined. The experimental work has been conducted here by Swamy and Al-Asali (1990) who investigated the chemical interaction for different percentage of fly ash in concrete mixture. They tested three different sets of beams with different kinds of reactive aggregates. The beam was simply supported and its total length was 800 mm. The geometry of the problem and position of longitudinal and shear reinforcement are given in Fig. 12. For this study one of the beams, referred to as "B3" by Swamy and Al-Asali (1990), has been selected and the obtained results compared

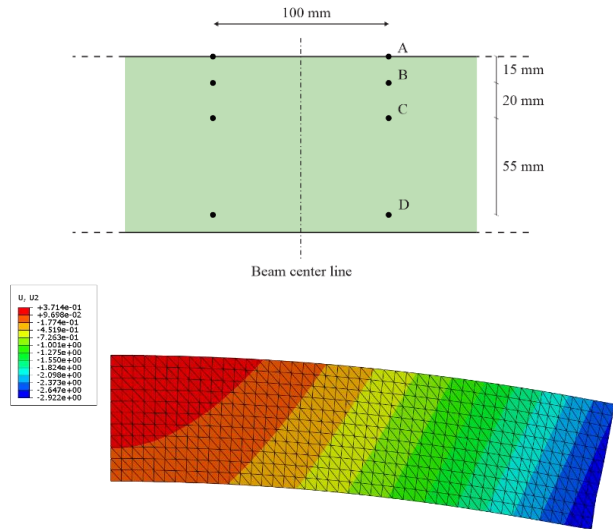


Fig. 13 (top) Selected points for measuring strain in concrete; (bottom) Deformation of the right half of concrete beam after 2 years of ASR

Table 1 Material properties of concrete and steel

Concrete modulus of elasticity	$E_c=30$ GPa
Concrete Poisson's ratio	$\nu=0.18$
Tensile strength of concrete	$f_t=1.8$ MPa
Concrete ASR constant	$A_1=20$ days
Steel modulus of elasticity	$E_s=200$ GPa
Steel Poisson's ratio	$\nu=0.2$
Steel yield stress	$f_y=560$ MPa
Maximum free expansion	$\varepsilon_x=1\%$

with the experiments. In view of the symmetry of the problem, only one half of beam was simulated. Material properties for concrete and reinforcement are summarized in the Table 1.

The beam has been placed in the environment with the controlled humidity and temperature for two years. The deformation was measured in both the reinforcement and concrete at the set of selected points, as shown in Fig. 13.

In the first stage of the test, i.e., in the two years' time interval, no external load was applied. Since the longitudinal reinforcement in the tensile region was more intense than that in the compressive zone, the beam has initially experienced an upward movement. In addition, as the compressive stress was increasing in the bottom layer, less chemical expansion occurred in the longitudinal direction, which lead to an increase in the curvature of beam. The final deformation after two years of progressive ASR is plotted in Fig. 13. The numerical simulations give similar results to laboratory tests as the total hogging of beam is reported to be about 3 mm.

In Fig. 14, the evolution of strain in the longitudinal tensile steel bar and concrete is plotted versus time. The experimental data was collected using the strain gages that were placed directly on steel rebars as well as at the surface of the beam, to monitor the deformation history. As it can be seen, during the first 100 days of continuing reaction the reinforcement elongates and then the expansion stops due to

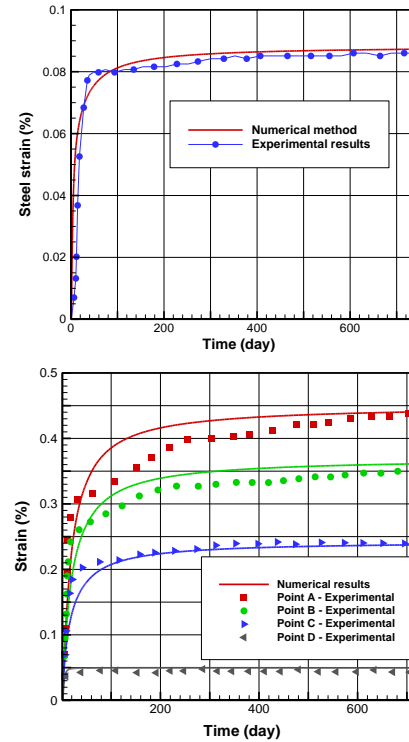


Fig. 14 Strain variation in steel (top) and concrete (bottom) in time

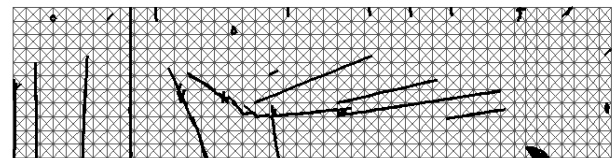
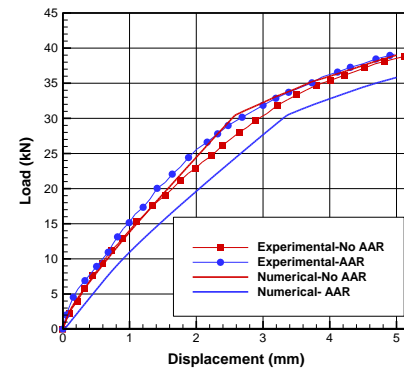


Fig. 15 (Top) Load vs displacement curve; (Bottom) crack pattern in 2D for the right half of beam

the generation of compressive stress in the bottom layer of the beam. The second plot in Fig. 14 shows the variation of strain within the concrete during the first two years of the reaction. Again, the numerical results are quite consistent with the experimental data for all points at which the measurements were taken.

The next stage of the experiment involved four-point bending of beams affected by ASR as well as the beam without any reactive aggregate. The corresponding load-displacement curves are shown in Fig. 15. It is noted that for the beam considered here (i.e., 'B3'; Beltane opal as

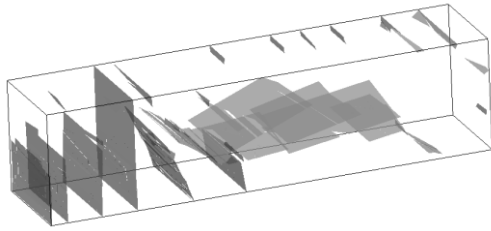


Fig. 16 Crack pattern in 3D (the right half of the beam)

reactive aggregate and 30% of fly ash as cement replacement) the stiffness recorded in the experimental test was virtually the same (or even marginally higher) as compared to that of the control beam with no ASR. In general, however, all the other results reported by Swamy and Al-Asali (1990) show that ASR substantially reduces both the stiffness and the flexure capacity of the beams. The latter is consistent with the numerical results which show a similar trend that can be attributed to progressive degradation in mechanical properties triggered by ASR.

Finally, the predicted crack pattern, at the end of simulation, is shown in Figs. 15 and 16. The most intense damage is in the tensile zone in the area adjacent to the reinforcement.

6. Conclusions

In this work, the chemo-mechanical formulation for describing the damage propagation in concrete affected by ASR has been presented. Within this framework two key effects of the chemical interaction, i.e., expansion of silica gel and degradation of strength/stiffness properties of concrete, were taken into account and an implicit algorithm has been presented for integration of the chemo-elastic constitutive relation.

The evolution of damage has been described using the concept of volume averaging, which discriminates between properties of the intact material and those of the interface and incorporates the characteristic length. The Rankine's criterion was used to define the onset of cracking. For tracing the crack path, a general three dimensional algorithm has been developed by employing tetrahedral elements and assuming that the crack is represented by a planar discontinuity surface formed within each element. For macroscopic description of cohesive cracks, the traction-separation law was formulated using a decaying exponential function which attenuated traction on crack faces during an active loading process.

Three different numerical examples have been provided to illustrate the proposed methodology. The first two involved an L-shaped plain concrete panel and a reinforced concrete beam subjected to mechanical loads. For both these cases, the load-displacement characteristics and the fracture pattern were compared with the experimental data. The last example dealt with examining the effects of ASR in a reinforced concrete beam. Again, the results were compared with the experimental evidence and clearly demonstrated the predictive abilities of the outlined framework.

References

- Bazant, Z.P. and Steffens, A. (2000), "Mathematical model for kinetics of alkali-silica reaction in concrete", *Cement Concrete Res.*, **30**(3), 419-428.
- Bazant, Z.P., Zi, G. and Meyer, C. (2000), "Fracture mechanics of ASR in concretes with waste glass particles of different sizes", *J. Eng. Mech.*, ASCE, **126**(3), 226-232.
- Belytschko, T. and Tabbara, M. (1993), "H-adaptive finite-element methods for dynamic problems, with emphasis on localization", *Int. J. Numer. Meth. Eng.*, **36**(24), 4245-4265.
- Berra, M., Faggiani, G., Mangialardi, T. and Paolini, A.E. (2010), "Influence of stress restraint on the expansive behaviour of concrete affected by alkali-silica reaction", *Cement Concrete Res.*, **40**(9), 1403-1409.
- Bresler, B. and Scordelis, A.C. (1963), "Shear strength of reinforced concrete beams", *ACI J. Proc.*, **60**(1), 51-74.
- Capra, B. and Bournazel, J.P. (1998), "Modeling of induced mechanical effects of alkali-aggregate reactions", *Cement Concrete Res.*, **28**(2), 251-260.
- Devloo, P. (1991), "A three-dimensional adaptive finite element strategy", *Comput. Struct.*, **38**(2), 121-130.
- Diamond, S. and Thaulow, N. (1974), "A study of expansion due to alkali-silica reaction as conditioned by the grain size of the reactive aggregate", *Cement Concrete Res.*, **4**(4), 591-607.
- Dumstorff, P. and Meschke, G. (2007), "Crack propagation criteria in the framework of X-FEM-based structural analyses", *Int. J. Numer. Anal. Meth. Geomech.*, **31**(2), 239-259.
- Gasser, T.C. and Holzapfel, G.A. (2006), "3d crack propagation in unreinforced concrete.: A two-step algorithm for tracking 3d crack paths", *Comput. Meth. Appl. Mech. Eng.*, **195**(37), 5198-5219.
- Haghighat, E. and Pietruszczak, S. (2015), "On modeling of discrete propagation of localized damage in cohesive-frictional materials", *Int. J. Numer. Anal. Meth. Geomech.*, **39**(16), 1774-1790.
- Haghighat, E. and Pietruszczak, S. (2016), "On modeling of fractured media using an enhanced embedded discontinuity approach", *Ext. Mech. Lett.*, **6**, 10-22.
- Hillerborg, A., Mod er, M. and Petersson, P.E. (1976), "Analysis of crack formation and crack growth in concrete by means of fracture mechanics and finite elements", *Cement Concrete Res.*, **6**(6), 773-781.
- J ager, P., Steinmann, P. and Kuhl, E. (2008), "Modeling three-dimensional crack propagation- A comparison of crack path tracking strategies", *Int. J. Numer. Meth. Eng.*, **76**(9), 1328-1352.
- Larive, C. (1998), "Apports combin es de l'exp erimentation et de la mod elisation   la comprehension de l'alcali reaction et de ses effets m caniques.", Laboratoire Central des Ponts et Chauss es (LCPC), Paris, France.
- L ger, P., Cote, P. and Tinawi, R. (1996), "Finite element analysis of concrete swelling due to alkali-aggregate reactions in dams", *Comput. Struct.*, **60**(4), 601-611.
- Linder, C. and Armero, F. (2007), "Finite elements with embedded strong discontinuities for the modeling of failure in solids", *Int. J. Numer. Meth. Eng.*, **72**(12), 1391-1433.
- Manzoli, O.L. and Shing, P.B. (2006), "A general technique to embed non-uniform discontinuities into standard solid finite elements", *Comput. Struct.*, **84**(10), 742-757.
- Mariani, S. and Perego, U. (2003), "Extended finite element method for quasi-brittle fracture", *Int. J. Numer. Meth. Eng.*, **58**(1), 103-126.
- Moallemi, S. and Pietruszczak, S. (2017), "Analysis of localized fracture in 3D reinforced concrete structures using volume averaging technique", *Finite Elem. Anal. Des.*, **125**, 41-52.
- Mo s, N. and Belytschko, T. (2002), "Extended finite element

- method for cohesive crack growth”, *Eng. Fract. Mech.*, **69**(7), 813-833.
- Moës, N., Dolbow, J. and Belytschko, T. (1999), “A finite element method for crack growth without remeshing”, *Int. J. Numer. Meth. Eng.*, **46**(1), 131-150.
- Multon, S., Cyr, M., Sellier, A., Leklou, N. and Petit, L. (2008), “Coupled effects of aggregate size and alkali content on ASR expansion”, *Cement Concrete Res.*, **38**(3), 350-359.
- Oliver, J. (1996), “Modelling strong discontinuities in solid mechanics via strain softening constitutive equations. Part 1: Fundamentals”, *Int. J. Numer. Meth. Eng.*, **39**(21), 3575-3600.
- Oliver, J., Huespe, A.E. and Sanchez, P.J. (2006), “A comparative study on finite elements for capturing strong discontinuities: E-FEM vs X-FEM”, *Comput. Meth. Appl. Mech. Eng.*, **195**(37), 4732-4752.
- Pan, J., Feng, Y., Jin, F., Zhang, C. and Owen, D.R.J. (2014), “Comparison of different fracture modelling approaches to gravity dam failure”, *Eng. Comput.*, **31**(1), 18-32.
- Pan, J., Feng, Y., Jin, F. and Zhang, C. (2013), “Numerical prediction of swelling in concrete arch dams affected by alkali-aggregate reaction”, *Eur. J. Environ. Civil Eng.*, **17**(4), 231-247.
- Pan, J., Feng, Y., Wang, J., Sun, Q., Zhang, C. and Owen, D. (2012), “Modeling of alkali-silica reaction in concrete: a review”, *Front. Struct. Civil Eng.*, **6**(1), 1-18.
- Pan, J., Zhang, C., Xu, Y. and Jin, F. (2011), “A comparative study of the different procedures for seismic cracking analysis of concrete dams”, *Soil Dyn. Earthq. Eng.*, **31**(11), 1594-1606.
- Pietruszczak, S. (1996), “On the mechanical behaviour of concrete subjected to alkali-aggregate reaction”, *Comput. Struct.*, **58**(6), 1093-1097.
- Pietruszczak, S. (1999), “On homogeneous and localized deformation in water-infiltrated soils”, *Int. J. Damage Mech.*, **8**(3), 233-253.
- Pietruszczak, S. and Haghghat, E. (2013), “Assessment of slope stability in cohesive soils due to a rainfall”, *Int. J. Numer. Anal. Meth. Geomech.*, **37**(18), 3278-3292.
- Pietruszczak, S. and Mroz, Z. (1981), “Finite-element analysis of deformation of strain-softening materials”, *Int. J. Numer. Meth. Eng.*, **17**(3), 327-334.
- Pietruszczak, S., Ushaksaraei, R. and Gocevski, V. (2013), “Modelling of the effects of alkali-aggregate reaction in reinforced concrete structures”, *Comput. Concrete*, **12**(5), 627-650.
- Sancho, J.M., Planas, J., Cendon, D.A., Reyes, E. and Galvez, J.C. (2007), “An embedded crack model for finite element analysis of concrete fracture”, *Eng. Fract. Mech.*, **74** (1), 75-86.
- Saouma, V. and Perotti, L. (2006), “Constitutive model for alkali-aggregate reactions”, *ACI Mater. J.*, **103**(3), 194-202.
- Sellier, A., Bourdarot, E., Multon, S., Cyr, M. and Grimal, E. (2009), “Combination of structural monitoring and laboratory tests for assessment of alkali-aggregate reaction swelling: Application to gate structure dam”, *ACI Mater. J.*, **106**(3), 281-290.
- Simo, J.C., Oliver, J. and Armero, F. (1993), “An analysis of strong discontinuities induced by strain-softening in rate-independent inelastic solids”, *Comput. Mech.*, **12**(5), 277-296.
- Sukumar, N., Moes, N., Moran, B. and Belytschko, T. (2000), “Extended finite element method for three-dimensional crack modelling”, *Int. J. Numer. Meth. Eng.*, **48**(11), 1549-1570.
- Swamy, R.N. and Al-Asali, M. (1990), “Control of alkali-silica reaction in reinforced concrete beams”, *ACI Mater. J.*, **87**(1), 38-46.
- Ulm, F.J., Coussy, O., Li, K.F. and Larive, C. (2000), “Thermo-chemo-mechanics of ASR expansion in concrete structures”, *J. Eng. Mech.*, ASCE, **126** (3), 233-242.
- Wells, G.N. and Sluys, L.J. (2001), “A new method for modelling cohesive cracks using finite elements”, *Int. J. Numer. Meth. Eng.*, **50**(12), 2667-2682.
- Winkler, B., Hofstetter, G. and Niederwanger, G. (2001), “Experimental verification of a constitutive model for concrete cracking”, *Proc. Inst. Mech. Eng., Part L: J. Mater. Des. Appl.*, **215**(2), 75-86.
- Winnicki, A., Serega, S. and Norys, F. (2014), “Chemoplastic modelling of alkali-silica reaction (ASR)”, *Comput. Model. Concrete Struct. (EURO-C)*, **2**, 765-774.
- Zienkiewicz, O.C., Huang, M.S. and Pastor, M. (1995), “Localization problems in plasticity using finite-elements with adaptive remeshing”, *Int. J. Numer. Anal. Meth. Geomech.*, **19**(2), 127-148.

HK